Proceedings of ASME Turbo Expo 2020
Turbomachinery Technical Conference and Exposition
GT2020
June 22-26, 2020, London, England

GT2020-15073

IMPROVED DELAYED DETACHED EDDY SIMULATION (IDDES) OF A 1.5 STAGE AXIAL COMPRESSOR NON-SYNCHRONOUS VIBRATION

Purvic Patel[*]
Yunchao Yang[†]
Gecheng Zha[‡]
Department of Mechanical and Aerospace Engineering
University of Miami
Coral Gables, Florida 33124
Email: gzha@miami.edu

ABSTRACT

This paper utilizes the Improved Delayed Detached Eddy Simulation (IDDES) to investigate the non-synchronous vibration (NSV) mechanism of a 1.5 stage high-speed axial compressor. The NSV occurs at a part speed in the rig test. A low diffusion E-CUSP Riemann solver with a third order Weighted Essentially Non-Oscillating (WENO) scheme for the inviscid flux and a second order central differencing scheme for the viscous flux are employed ~~in~~ 3D time accurate Navier-Stokes ~~solver.~~ The ~~time-step based on the~~ fully conservative sliding boundary condition is used to preserve the wake-propagation. The aerodynamic instability in the tip region induces two alternating low pressure regions near the leading and the trailing edge on the suction side of the rotor blade. ~~Its trajectory~~ in the rotor passage above 75 % span and its coupling forces cause NSV at the operating speed. This instability moves in the counter-rotating direction in the rotational frame. The NSV results using URANS simulation is also presented for comparison. The predicted frequency with the IDDES and URANS using rigid blades agrees well with the measured frequency in the rig test. In addition to the NSV, IDDES captures dominant engine order frequencies ~~as compared to the URANS~~. The tip flow ~~structure shows~~ the vortex filament with one end on the suction side of the rotor blade and other side terminating on the casing or the pressure side of the rotor blade.

NOMENCLATURE

L_{ref}	Reference length
d_w	Wall normal distance
ρ_∞	Freestream density
U_∞	Freestream velocity
μ_∞	Freestream dynamics viscosity
Ω	Vorticity / Rotational speed of a rotor
Re	Reynolds number
Ro	Rossby number
LE	Leading Edge
TE	Traling Edge
SS	Suction Surface
PS	Pressure Surface
TV	Tornado-like Vortex
RV	Radial Vortex
WENO	Weighted Essentially Non-Oscillating
NSV	Non-Synchronous Vibration
SFV	Separated Flow Vibration
SA	Spalart-Allmaras
RANS	Reynolds-Averaged Navier-Stokes
URANS	Unsteady Reynolds-Averaged Navier-Stokes
DDES	Delayed Detached-Eddy Simulation
IDDES	Improved Delayed Detached-Eddy Simulation

[*]Ph.D. Student
[†]Currently Postdoctoral Research Associate at the University of Florida
[‡]Professor, ASME Fellow

Copyright © 2020 by ASME

LES Large Eddy Simulation

INTRODUCTION

Over the years, axial compressor stage pressure ratio continues to increase to meet the aviation industry demands for improving efficiency, lighter weights, etc. This increased blade loading makes it necessary at the early design phase to tackle the various aero-mechanics problems. The forced and self-excited vibrations have been studied historically and somewhat understood. Another aero-mechanics problem of non-engine order vibration, namely Non-Synchronous Vibration (NSV), has grabbed more attention recently and is still not fully understood. During the NSV, the compressor operates in the stable operating range and a rotor blade experiences unsteady blade loading. It may create high amplitude unsteady blade loading that leads to the High Cycle Fatigue (HCF) failures. Consequently, the full comprehension of the NSV can help the compressor designer to circumvent the costly repair or design modifications later.

The experimental work of Mailach et al. [1], März et al. [2], Kielb et al. [3] shows the role of tip flow instability for the NSV. In the experimental and numerical work of Kielb et al. [3] on a high-speed axial compressor, the NSV consists of two coupled aerodynamic instabilities i.e., suction side vortex separation and tip flow instability. The global properties like pressure ratio and mass flow rate oscillates at the NSV frequency. In the case of tip flow instability driven NSV, the tip clearance size or shape also affects the NSV frequency and amplitude [2, 4] apart from the inlet temperature [5].

Möller et al. [6] carried out numerical investigation on a 1-1/2 stage axial compressor to understand the NSV mechanism. Based on their study, the vibration phenomenon is similar to the flutter and caused by the tip flow instability. The blockage near the casing enables tip clearance flow to travel backward multiple blade passages in rotational frame before impinging on the blade pressure side and thereby vibration is not only affected by the adjacent blade itself. With the reduced tip clearance, the excitation is alleviated due to the reduced tip clearance flow.

The experimental work of Brandstetter et al. [7] on high pressure axial compressor shows the transient flow structures and its relation to the NSV. The backward traveling aerodynamic disturbance in the rotational frame is observed during the NSV period. The multiple harmonics at frequencies other than the blade natural frequencies are detected due to non-linear blade vibrations. The phase-locked mechanism between aerodynamic and structural disturbance is seen with the increased vibration along with the broadband disturbance. This phase-locked mechanism for the NSV is also described by Spiker et al. [8]. The propagation of Radial Vortices (RVs) is determined by aerodynamics and these RVs / vortical spike flow structure [9] is developed by the leading edge flow separation due to the high incidence.

The full-annulus numerical simulation by Espinal et al. [10] on a high-speed 1-1/2 stage compressor shows the NSV is a full-annulus phenomenon with a vortex core line in every rotor-blade passage near and in front of the leading edge of the blades. They observe the presence of Separated Flow Vibrations (SFV) apart from the dominant NSV as observed in the rig test casing unsteady pressure measurement and some blades exhibit different NSV frequencies. Based on both of these studies using rigid blades, the tip flow instability in the upper span region induces the NSV.

Most of the previous numerical NSV studies [3, 4, 10–15] have focused on using an Unsteady Reynolds-Averaged Navier-Stokes (URANS) to reduce computational efforts and time. Even though URANS can fairly resolve the NSV frequency caused by the lumped aerodynamic force, the vortex structure may not be fully resolved due to its diffusive nature. It can reasonably capture the long-term periodic oscillation, but most of the one and two-equation based models have failed to predict the separation properly as they rely on modeling all scale eddies instead of resolving. At off-design speed, the compressor stage encompasses separation and complex vortical flows. The URANS being overly diffusive in nature fails to predict separation properly and doesn't capture small scale eddy structures. Therefore, a high-fidelity turbulence model is beneficial to resolve the tip flow instability and associated vortex flows. Even though Large Eddy Simulation (LES) resolves large eddy structures and models the effect of more isotropic small eddies, the excessive computational resources and time prohibits its usage for high Reynolds number industrial applications.

A hybrid turbulence model combining the advantages of RANS and LES methodologies is thus attractive. In 1997, Spalart et al. proposed such a model, called Detached-Eddy Simulation (DES), based on the one-equation Spalart-Allmaras model. Owing to its RANS/LES interface switch as a function of local grid size, it suffers from the Grid-Induced Separation (GIS) or Modeled-Stressed Depletion (MSD) problem under an ambiguous grid. This model has gone through improvements that led to the development of Delayed Detached-Eddy Simulation (DDES) [16] and subsequently Improved Delayed Detached-Eddy Simulation (IDDES). Liu et al. [17] investigates an axial compressor tip leakage vortex using the URANS and the DDES. In their study the DDES captures the tip leakage vortex more closer to the experiment. The study by Kelly et al. [18] shows that the hybrid turbulence improves turbomachinery flow performance prediction even on the RANS-type grid densities.

The objective of this paper is to employ the high-fidelity IDDES turbulence model to investigate the NSV of a high-speed axial compressor based on rigid rotor blades. The vortex structure and flow pattern in the tip region are analyzed and compared with the URANS results. The predicted tip vortex instability with more detailed structures can shed more ~~lights~~ light on the NSV mechanism.

Copyright © 2020 by ASME

COMPRESSOR

A 1-1/2 stage high-speed compressor of GE is investigated in this paper. Figure 1 shows a meridional view of the 1-1/2 stage blades, which has 56 IGV blades, 35 Rotor blades and 70 Stator blades. The tip clearance is 1.1 % tip chord. The compressor rotor blades are mounted in dovetail arrangement. Its rotor blades exhibits the NSV of the 1T mode [3,4,10,13,19–21] in the speed range of 12,700 rpm to 12,880 rpm. For the present study, only one-seventh sector is considered to represent the 5 nodal diameters observed in the testing as simulated by Im et al. [4]. Such a 1/7th sector treatment is verified by the full annulus NSV simulation of Espinal et al. [10].

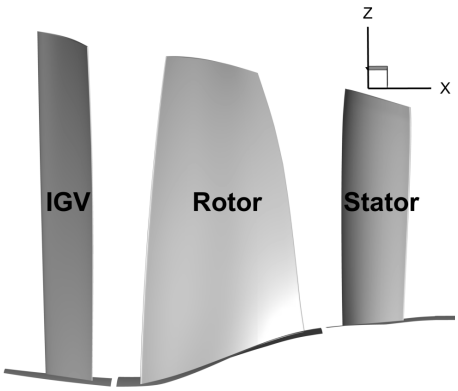

FIGURE 1: Geometry

NUMERICAL METHODS

The unsteady filtered compressible Navier-Stokes equations are solved for the hybrid IDDES model [22]. The URANS algorithm for the NSV is described by Im et al in [4]. These equations are nondimensionalized using L_{ref}, ρ_∞, U_∞ and μ_∞. The detailed implementation of these models can be found in refs. [4, 22]. An implicit unfactored Gauss-Seidel line iteration method is employed with the dual-time stepping scheme after Jameson [23] owing to its stability and robustness. In this scheme, a second order backward differencing scheme is employed for the unsteady term involving the physical time step whereas the pseudo time-step is discretized using a first-order Euler scheme.

A low-diffusion ECUSP scheme [24] originated from the flux vector splitting scheme of Zha and Bilgen [25] is used for the inviscid flux, where the conservative variables at the cell interface are constructed with a third-order WENO scheme. The viscous flux at the interface is reckoned with a second-order central differencing scheme.

At the inlet, the radial distributions of total pressure, total temperature, swirl angle and pitch angle are specified. A component of velocity is extracted from the inner domain to calculate remainder conservative variables. The radial distribution of static pressure is applied at the outlet. Due to the subsonic flow at the outlet, velocity components and turbulence quantity are extrapolated from the computational domain. The density is determined using an isentropic relation. The no-slip wall boundary condition is employed on blade surface, whereas the remaining walls are modeled with an efficient wall BC, which switches from the no-slip to wall function approach if y^+ is between 11 and 300. In addition, a zero heat flux through the wall is imposed with an adiabatic relation. For the rotating walls, the wall static pressure contribution in the inviscid momentum equation is ascertained by solving the radial equilibrium and the zero static pressure gradient is considered for the stationary walls. At the periodic boundaries, the time-shifted phase lag BC with a nodal diameter (ND) of 5 is applied using the direct store method [13]. The rationale for using ND5 is related to the observed NSV of ND5 with the backward traveling wave in the rotational frame. A fully conservative sliding BC [26] is applied between the blade rows to capture wake propagation, shock interaction, and vortex instabilities. The compressor operating speed is 12,880 rpm, where the NSV is observed in the rig test.

A non-dimensional time-step of about 0.005 is used. It corresponds to approximately 20 times the Blade Passing Frequency (BPF) of the stator and is determined by

$$\Delta t = \frac{2\pi}{Ro \times N_c} \tag{1}$$

where, N_c denotes total number of time steps in one rotor revolution. The rotor rotates one circumferential grid per time step. This ensures one-to-one mesh connection at the blade row interface required by the fully conservative sliding BC. In each physical time-step, the L2-norm residual is reduced by two orders of magnitude, which usually requires 25 to 35 pseudo time-step iterations. The computation is carried out for 13 revolutions.

IDDES subgrid length-scale

The sub-grid length scale for the SA-IDDES turbulence model is written as:

$$\Delta = \min\{\max[C_w d_w, C_w h_{max}, h_{wn}], h_{max}\} \tag{2}$$

where, d_w is the nearest wall distance, h_{wn} is the wall-normal grid size, h_{max} is the maximum local grid step, and the empirical constant C_w is 0.15.

Particular attention needs to be given to the h_{wn} term in Equation (2). In Figure 2, the ordinate represents the sub-grid

Copyright © 2020 by ASME

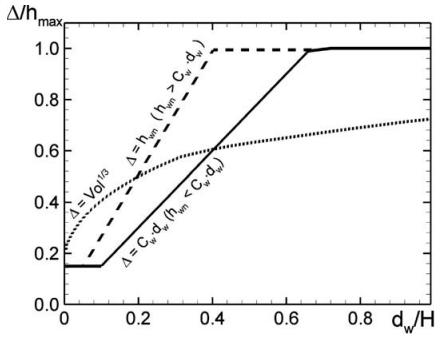

FIGURE 2: IDDES subgrid length-scale [27]

length scale normalized by h_{max} and the abscissa represents the wall-normal distance normalized by a plane channel half-width H. Depending on h_{wn} value, the sub-grid length scale can assume two possible variations. If $h_{wn} \leq C_w d_w$, $\Delta = C_w h_{max}$ as long as $d_w < h_{max}$. It grows linearly for $d_w > h_{max}$ till it reaches the value of h_{max} and then remains constant. For another scenario, i.e., $h_{wn} > C_w d_w$, initially Δ remains equal to $C_w h_{max}$ for $h_{wn} < C_w h_{max}$. Then it grows linearly at a rate higher than C_w until the maximum value of h_{max} and then remains constant. Based on Shur et al. [27], the second possibility is undesirable situation but with any rate of wall-normal step stretching that is acceptable for an accurate LES, it still does not lead to disaster.

COMPUTATIONAL GRID

A one-seventh sector computational grid is shown Figure 3. The O-mesh topology is used around the blades to maintain highly orthogonal grid near the walls and improve convergence. The H-mesh topology is used for the blade row interface blocks and for the extended domain at the inlet and outlet. These interface blocks are used between the blade rows for the fully conservative sliding BC. The computational grid for the IGV and the stator blade has the grid points of 121 around the blade and 51 normal to the blade and 71 in the radial direction. The O-mesh topology around the rotor blade consists of 201 points around the blade, 51 points normal to the blade and 71 points in the radial direction. The tip-block is fully gridded with O-mesh topology and 21 grid points in the radial direction. The computational domain contains a total number of 11,886,560 cells. The computational domain is split into 178 blocks for high-scalability parallel computing. The grid convergence study is carried out by Im et al. [4].

NUMERICAL PROBES

In Figure 4, the intersection of two lines represents one numerical probe location. There are 15 numerical probes installed on the suction surface of a rotor blade and similarly on the pres-

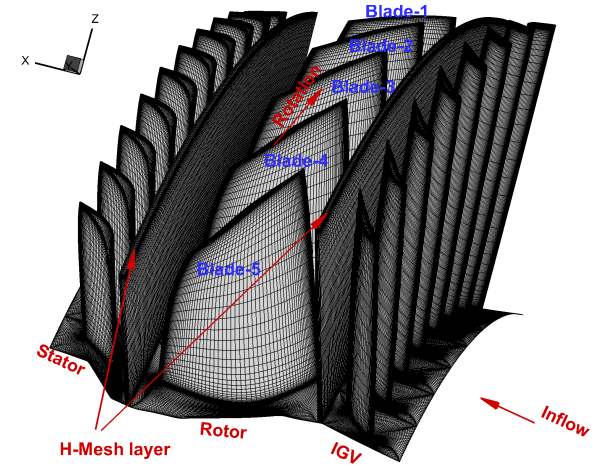

(a) One-seventh sector mesh

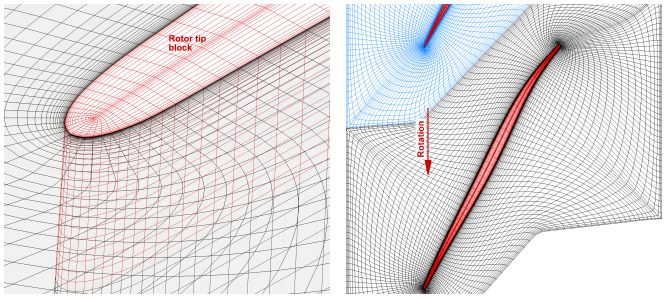

(b) Tip block (c) Blade to blade mesh

FIGURE 3: Mesh overview [19]

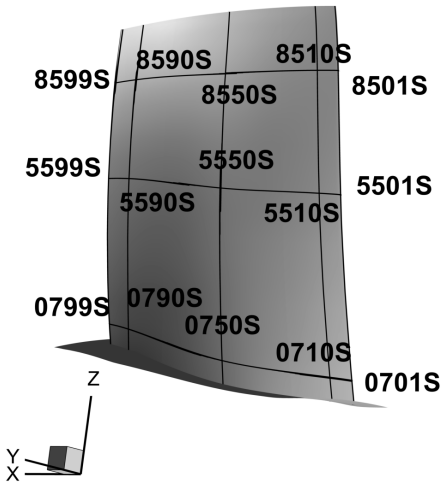

FIGURE 4: Numerical probes on SS of Rotor blade

Copyright © 2020 by ASME

sure surface. Each probe location for a blade is uniquely identified by four digits and an alphabet. First two numerals describe spanwise location, remaining two digits represent its axial location in terms of percentage chord length from the leading edge and an alphabet describes suction (S) or pressure (P) side. A total number of 30 probes capture the instantaneous static pressure over a blade surface. The pressure side numerical probes are not shown in the figure however their locations are identical to the suction surface.

RESULTS ANS DISCUSSION

It should be noted that the unsteady calculation is started from the steady-state converged results obtained using a mixing plane approach between the blade rows. The computed operating point and the Fast Fourier Transform (FFT) analysis of an unsteady pressure signal are carried out based on last three revolutions to avoid initial flow transition effects.

Campbell Diagram

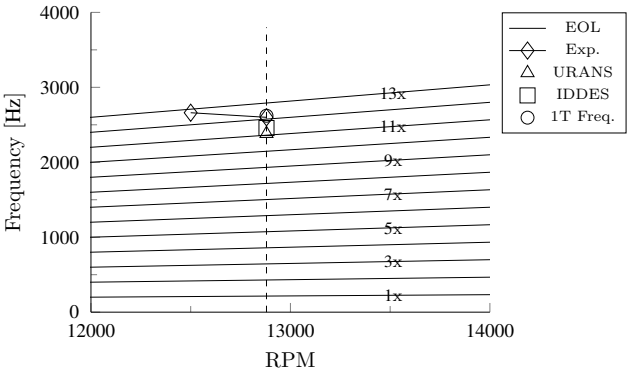

FIGURE 5: Campbell diagram

The predicted NSV frequency with the URANS and IDDES is marked on the Campbell diagram, Figure 5. The vertical line represents the rotor speed used in the present study. The experimentally measured NSV and the second natural vibration frequency of the rotor blade are also marked and they are between 12 and 13 EOL. The radially outward fanning lines from the origin correspond to the Engine Order Line (EOL). The IDDES turbulence model predicts the NSV frequency of 2457 Hz as compared to 2381.4 Hz by the URANS and they are residing between 11 and 12 EOL. These frequencies are based on the Blade-4 Suction side numerical probe 8510S.

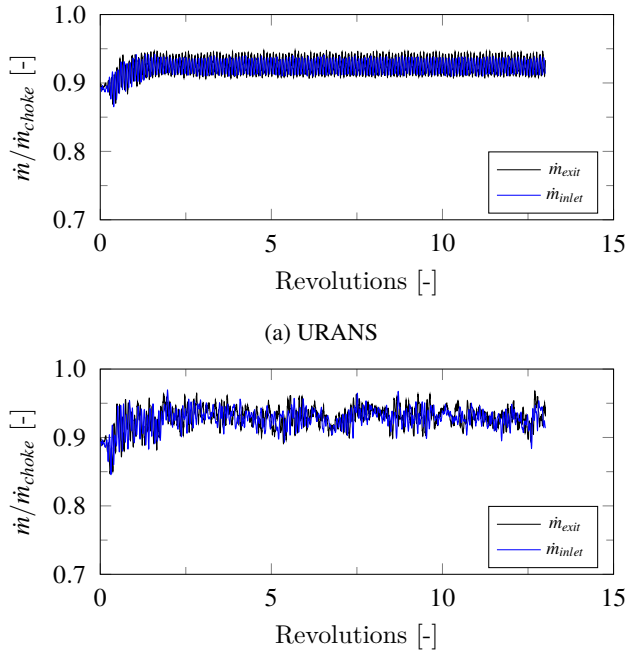

(a) URANS

(b) IDDES

FIGURE 6: Mass flow rate variation

Mass flow rate variation

The nondimensional mass flow rate with the two different turbulence models is compared in Figure 6. The mass flow rate is normalized with the steady-state choked mass flow rate. The mass flow rate at the IGV inlet is denoted by $\dot{m}_{inlet}$ and $\dot{m}_{exit}$ refers to the rotor exit mass flow rate. With the URANS, the mass flow rate variation exhibits a typical Limit Cycle Oscillation (LCO) after approximately initial three revolutions whereas it oscillates with multiple frequencies with the IDDES. The complete breakdown of the mass flow rate is not observed which indicates the compressor operation is stable and not stalled. The averaged IGV inlet and rotor exit mass flow rate with the IDDES is approximately 0.31 % higher than the URANS. This averaged mass flow rate is calculated based on last three revolutions.

Excitation Frequencies

The strain gauge response of a rotor blade is shown in Figure 7. The peak in vibration amplitude are plotted in the Campbell diagram. As these gauges are more prone to respond near the blade natural frequencies, their response is strong near the blade vibration harmonics. This can be understood by comparing the amplitude of Separated Flow Vibration (SFV) between the strain gauge response (Figure 7) and the unsteady pressure measurement at the casing (Figure 8). In Figure 8, the frequencies associated with the unsteady pressure measurement are almost equi-

Copyright © 2020 by ASME

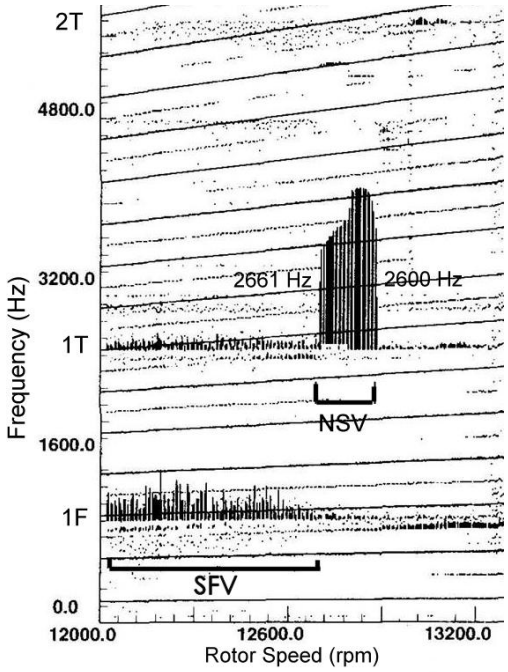

FIGURE 7: Strain gauge response of first stage rotor blades in a rig test [3]

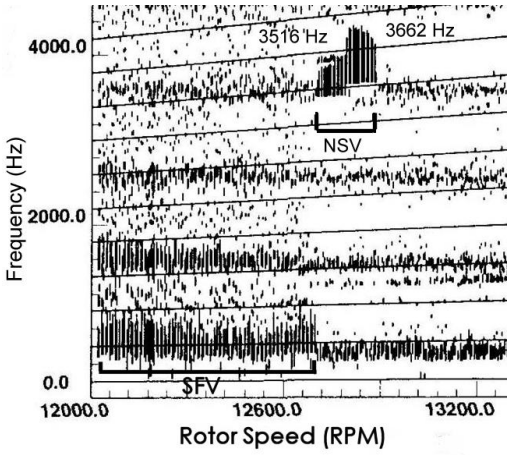

FIGURE 8: Casing unsteady pressure measurement [3]

spaced. The response frequencies in Figure 8 are doppler shifted from the rotational frame.

The unsteady static pressure measurements on one of the rotor blade surface with the different turbulence models are compared in Figure 9. These measurements are nondimensionalized using the freestream density and velocity. Similar to the mass flow rate variation, the URANS results exhibit a LCO behavior as against the IDDES. The amplitude of static pressure variation grows along the spanwise direction and remains almost same in the upper 20 % span due to the tip flow instability. This non-LCO type unsteady pressure is also observed by Patel et al. [21] and Gan et al. [28] on the same one-seventh sector with the Fluid-Structure Interaction (FSI) using the DDES and URANS turbulence model respectively. They observe that NSV is dominant based on the unsteady pressure response. In their FSI simulation, the first mode modal displacement has remained dominant with the URANS as well as the DDES in comparison to the experimentally measured second mode and the reason for the same is still being analyzed.

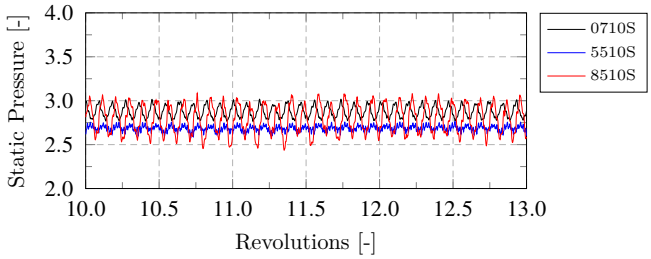

(a) URANS

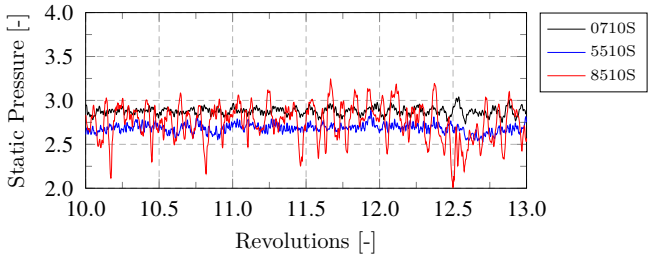

(b) IDDES

FIGURE 9: Instantaneous Blade-4 SS static pressure

The Fast Fourier Transform analysis using the Hanning window of the unsteady pressure signal is shown in Figure 10. The abscissa represents the frequency normalized with the first engine order frequency and the ordinate represent the amplitude. Both models predict the NSV between 11 and 12 engine order frequency. The magnitude of the NSV frequency with IDDES is approximately half of the URANS prediction. Based on the URANS results, the NSV amplitude is pronounced in all spanwise numerical probes and its magnitude drops approximately by half in the inverse radial direction. Based on the URANS, there is another non-engine order frequency at 85 % span location between 5 and 6 engine order frequency. However, the IDDES predicts 7th and 8th engine order frequency with the amplitude similar to the NSV frequency. In the case of IDDES, the energy associated with eddies is distributed among various frequencies as compared to the distinct frequency with the URANS. The IGV

Copyright © 2020 by ASME

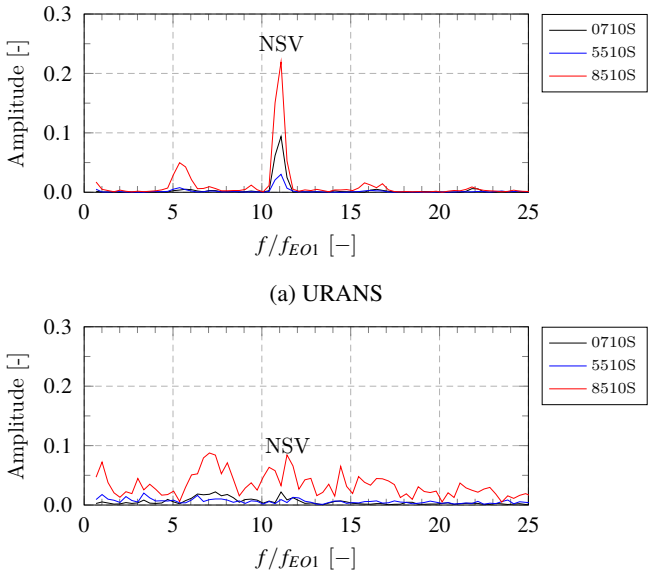

FIGURE 10: Frequency analysis of Blade-4 SS static pressure

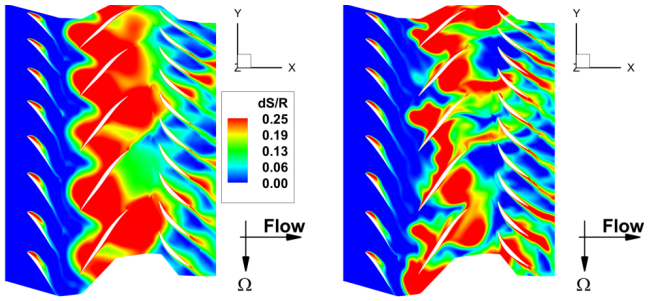

FIGURE 11: Entropy contour at 85 % span

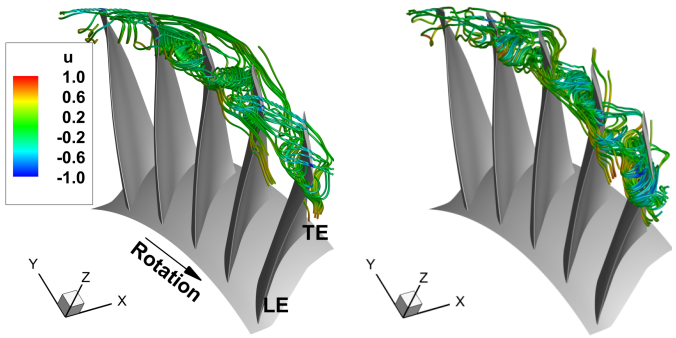

FIGURE 12: Rotor tip flow instability

blade passing frequency of 12,101 Hz, not shown here, is also captured by both of the models with the similar amplitude. Its magnitude is relatively much smaller as compared to other frequencies and remains constant at all radial location at 10 % axial chord location from the LE.

Flow Structure and Instabilities

Figure 11 ~~depicts~~ the nondimensional entropy contour at 85 % span location for both turbulence models. The wake propagation is fully conserved with the sliding conservative BC. The high entropy region boundary in the upstream of the rotor appears more like a wave form as compared to the IDDES. The rotor wake impinges on the stator blades and ~~its structure differs~~ vastly with the IDDES. Similarly the complex interaction of the IGV wake with the tip flow instability is different due to aperiodic flow structure near the rotor LE with the IDDES. This aperiodic flow strucutre with the IDDES causes the unsteady pressure signal to differ a lot between the different rotor blades over the same revolution range and therefore its frequency analysis leads to the peak at different frequencies for the rotor blades.

The tip flow structure with both turbulence models ~~is~~ compared in Figure 12. The instantaneous streamlines are contoured with the normalized axial velocity. A Tornado-like Vortex (TV) structure in the tip region is observed. It is generated near the LE of the rotor blade owing to the high-incidence angle. It creates a large flow blockage ~~and~~ due to its rotation about its own axis. A part of the main flow moves downstream by nudging it below. Near the LE and TE of the rotor, the tip flow moves circumferentially backward and crosses multiple blade passage before impinging on the pressure side of blade or merging with the tip flow instability which suggests that the aerodynamic instability affects not only to the adjacent blade. Möller et al. have also observed similar phenomenon for the non-synchronous vibration of a 1.5 stage axial compressor [6]. With the URANS, the vortex structure appears~~s~~ more organized in contrast to the chaotic flow with the IDDES.

To understand which aerodynamic instability causes the NSV in the present case, the vortex structure is tracked with the instantaneous streamlines as shown in Figure 13. The instantaneous streamlines are shown along with the normalized Q criterion (i.e. normalized with the freestream velocity and the tip chord of rotor blade) contour at 85 % span location. The high Q criterion value is associated with the vortex. In Figures 13 and 14, 0/70 to 6/70 denotes a few instants from the 12th revolutions. To track the vortex and its associated frequency, two reference lines are created (shown in green color), i.e. one near the vortex center and one near the outer edge of the vortex. It is observed that the vortex travels along the suction surface of the blade starting from the LE. Once it reaches the throat area,

Copyright © 2020 by ASME

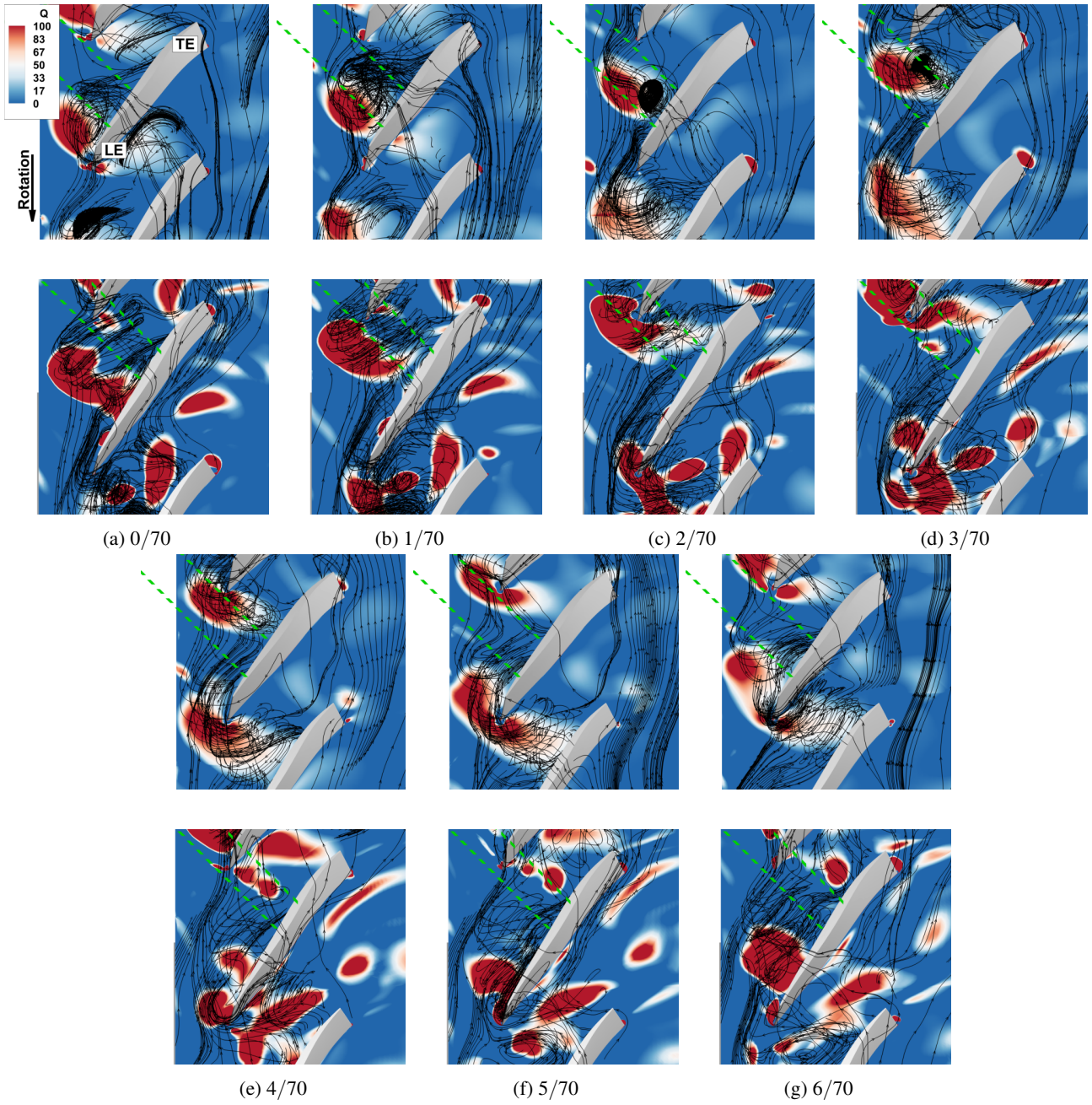

(a) 0/70 (b) 1/70 (c) 2/70 (d) 3/70

(e) 4/70 (f) 5/70 (g) 6/70

FIGURE 13: Vortex movement in the tip region of rotor (Top: URANS and Bottom: IDDES)

formed by the aft part of the current blade SS and the LE of the adjacent blade PS, it traverses the passage and moves to the LE of the adjacent blade PS. After reaching the PS, it moves to the LE of the current blade SS. This kind of vortex motion takes in between 6/70 to 7/70 rotor revolutions which corresponds to the approximate frequency between 2100 Hz and 2500 Hz. This frequency range matches with the predicted frequency by both the models. This kind of vortex movement generates two low pressure regions near the LE and TE of the rotor blade and their coupling force is responsible for the NSV near the 1T mode of the blade. Apart from the vortex motion, the IDDES displays the small scale vortex structure with the high-concentration of rotation rate relative to the strain rate.

The iso-surfaces of λ_2 vortex criterion are colored with the

Copyright © 2020 by ASME

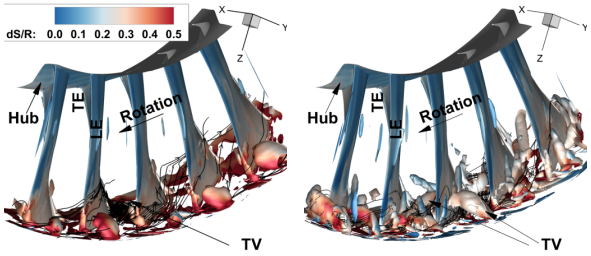

(a) 0/70

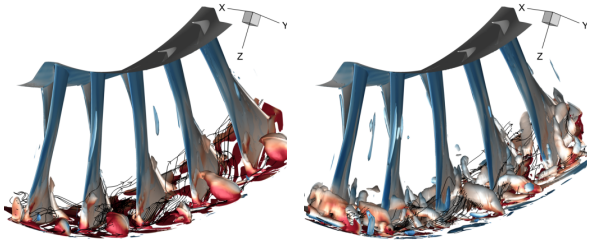

(b) 1/70

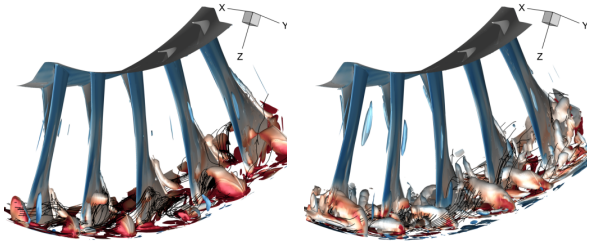

(c) 2/70

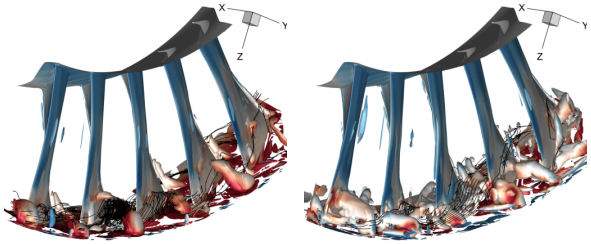

(d) 3/70

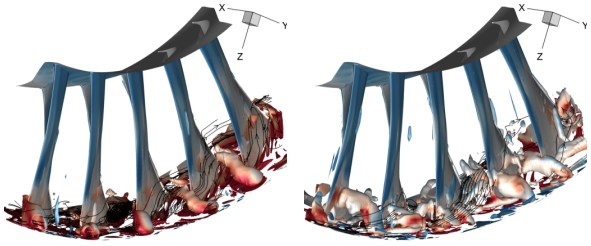

(e) 4/70

FIGURE 14: Iso-surfaces of $\lambda_2 = -35$ in the Rotor (Left: URANS and Right: IDDES)

nondimensional entropy in the Figure 14. A tornado-like vortex (TV) spanning from the rotor blade suction surface to the casing can be seen near the LE. Its one end moves along the suction surface and other end moves in the counter-rotating direction in the rotational frame over the time. Once it reaches near the LE of the adjacent blade, rotor blade cuts it and it interacts with the tip flow instability near the LE. This leads to the formation of the vortex filament between the SS of the current blade and the PS of the adjacent blade. The appearance of this vortex is more pronounced with the high-fidelity IDDES along with the small scale structure vortex.

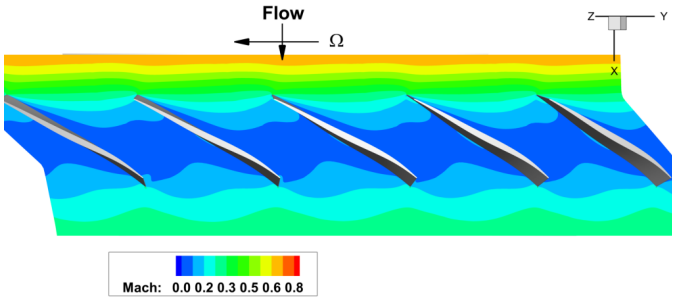

(a) URANS

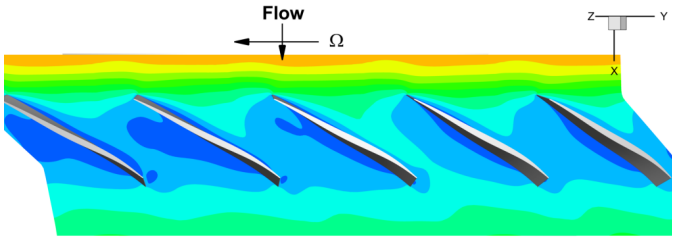

(b) IDDES

FIGURE 15: Time-averaged relative mach contour of rotor at 88 % span

Figure 15 compares the statistical time-averaged relative mach contour of last three revolutions. URANS predicts the periodic flow structure between different blade passages with the low axial momentum as compared to the aperiodic flow structure with the IDDES. The time-averaged aperiodic flow field suggests that the vibration response of different blades will vary based on the flow structure and the length of time-average.

Total Pressure Ratio Radial Profile

The statistical time-averaged total pressure ratio profile of last three revolutions across the rotor outlet and the IGV inlet is examined in Figure 16. This pressure ratio is based on the cir-

Copyright © 2020 by ASME

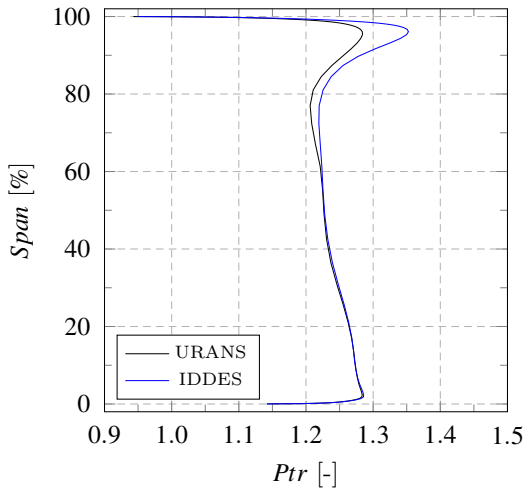

FIGURE 16: Time-averaged radial profile of total pressure ratio

cumferential mass averaged absolute total pressure. The difference in pressure ratio above 60 % span location is subtle with the maximum variation in the tip region. The blade loading above 75 % induces the high-incidence angle and thereby separation and the circumferentially traveling vortex. As the blade loading in the lower half span shows very little variation, it would be better to increase the loading and reduce in the upper span to alleviate the NSV. The IDDES appears to be closer to the tip stall than the URANS. The averaged total pressure ratio with the IDDES model is 0.7 % higher that the URANS based on the last three revolutions.

CONCLUSION

A one-seventh sector of a high-speed axial compressor is investigated for the ~~non-engine order~~ vibration using ~~the URANS and~~ the IDDES turbulence ~~models~~. Both models predict the NSV frequency fairly well. Following conclusions are drawn from the present study:

1 The aerodynamic instability above 75 % span induces the NSV.
2 The vortex trajectory in the upper span region creates low pressure regions near the LE and the TE of the rotor blade tip. Their coupling force causes the NSV near the first torsional mode of the blade.
3 The high-fidelity IDDES turbulence model predicts the more realistic chaotic nature of the turbulence along with the small scale eddies. An apperance of tornado-like vortex with filament spanning from casing to the rotor suction side is more pronounced along with the small scale eddies due to its LES like behavior in the tip flow instability.
4 The unsteady pressure signal with the IDDES doesn't exhibit a typical LCO and the energy associated with the eddies are distributed among the various length scale separations as compared to the URANS.
5 The IDDES predicts the engine order frequencies of ~~almost~~ similar amplitude along with the NSV as compared to the URANS.
6 The trajectory of the tip ~~flow instability~~ suggests that the vibration measured on the pressure side of the rotor blade is not only influenced by the adjacent blade itself.

ACKNOWLEDGMENT

All the computations were carried out using the computational resources of Center for Computational Science at University of Miami. We thank GE for approval of publishing the NSV research under the GUIde 4 program. We would also like to thank Dr. Robert Kielb from the Duke University for the valuable discussion on the NSV.

REFERENCES

[1] Mailach, R., Lehmann, I., and Vogeler, K., 2001. "Rotating instabilities in an axial compressor originating from the fluctuating blade tip vortex". *Journal of Turbomachinery,* ***123***(3), July.
[2] März, J., Hah, C., and Neise, W., 2002. "An experimental and numerical investigation into the mechanisms of rotating instability". *Journal of Turbomachinery,* ***124***(3), July, pp. 367–374.
[3] Kielb, R. E., Barter, J. W., Thomas, J. P., and Hall, K. C., 2003. "Blade excitation by aerodynamic instabilities: A compressor blade study". pp. 399–406. GT2003-38634.
[4] Im, H., and Zha, G., 2014. "Investigation of flow instability mechanism causing compressor rotor-blade nonsynchronous vibration". *AIAA Journal,* ***52***(9), pp. 2019–2031.
[5] Thomassin, J., Vo, H. D., and Mureithi, N. W., 2011. "The tip clearance flow resonance behind axial compressor nonsynchronous vibration". *Journal of Turbomachinery,* ***133***(4), Oct.
[6] Möller, D., Jüngst, M., Holzinger, F., Brandstetter, C., Schiffer, H.-P., and Leichtfuß, S., 2017. "Mechanism of Nonsynchronous Blade Vibration in a Transonic Compressor Rig". *Journal of Turbomachinery,* ***139***(1), 01.
[7] Brandstetter, C., Jüngst, M., and Schiffer, H.-P., 2018. "Measurements of radial vortices, spill forward, and vortex breakdown in a transonic compressor". *Journal of Turbomachinery,* ***140***(6), 04. TURBO-17-1218.
[8] Spiker, M. A., Kielb, R. E., Hall, K. C., and Thomas, J. P., 2008. "Efficient design method for non-synchronous vibrations using enforced motion". Vol. Volume 5: Structures and Dynamics, Parts A and B of *Turbo Expo: Power for Land, Sea, and Air*, pp. 735–747.

Copyright © 2020 by ASME

[9] Pullan, G., Young, A. M., Day, I. J., Greitzer, E. M., and Spakovszky, Z. S., 2015. "Origins and structure of spike-type rotating stall". *Journal of Turbomachinery,* ***137***(5), 05. TURBO-14-1202.

[10] Espinal, D., Im, H.-S., and Zha, G.-C., 2017. "Full-annulus simulation of nonsynchronous blade vibration excitation of an axial compressor". *Journal of Turbomachinery,* ***140***(3), 12. 031008.

[11] Sanders, A., 2005. "Nonsynchronous vibration (nsv) due to a flow-induced aerodynamic instability in a composite fan stator.(author abstract)". *Journal of Turbomachinery,* ***127***(2), Apr.

[12] Im, H.-S., and Zha, G.-C., 2012. "Effects of rotor tip clearance on tip clearance flow potentially leading to nsv in an axial compressor". pp. 1383–1394. GT2012-68148.

[13] Im, H.-S., and Zha, G.-C., 2012. "Simulation of non-synchronous blade vibration of an axial compressor using a fully coupled fluid/structure interaction". pp. 1395–1407. GT2012-68150.

[14] Clark, S. T., Besem, F. M., Kielb, R. E., and Thomas, J. P., 2015. "Developing a reduced-order model of non-synchronous vibration in turbomachinery using proper-orthogonal decomposition methods". *Journal of Engineering for Gas Turbines and Power,* ***137***(5), 05. 052501.

[15] Fiquet, A.-L., Brandstetter, C., Aubert, S., and Philit, M., 2018. "Non-engine order oscillations in an axial multi-stage compressor - aeroacoustic interaction". ISUAAAT15-087.

[16] Spalart, P. R., Deck, S., Shur, M. L., Squires, K. D., Strelets, M. K., and Travin, A. K., 2006. "A new version of detached-eddy simulation, resistant to ambiguous grid densities". *Theoretical and Computational Fluid Dynamics,* ***20***(3), May, p. 181.

[17] Liu, Y., Zhong, L., and Lu, L., 2019. "Comparison of DDES and URANS for Unsteady Tip Leakage Flow in an Axial Compressor Rotor". *Journal of Fluids Engineering,* ***141***(12), 06. 121405.

[18] Kelly, R., and Jemcov, A., 2018. "Application of a hybrid urans/les turbulence model to turbomachinery flows".

[19] Im, H., and Zha, G., 2014. "Investigation of non-synchronous vibration mechanism for a high speed axial compressor using delayed des". AIAA SciTech Forum. American Institute of Aeronautics and Astronautics, Jan.

[20] Patel, P., Im, H.-S., and Zha, G., 2019. *Numerical investigation of Non-Synchronous vibration using Scale Adaptive Simulation turbulence model*. Aug.

[21] Patel, P., Im, H.-S., and Zha, G., 2020. *Numerical Investigation of Non-Synchronous Vibration with Fluid-Structure Interaction using Delayed Detached Eddy Simulation*. Jan.

[22] Yang, Y., and Zha, G., 2016. "Simulation of airfoil stall flows using iddes with high order schemes". In 46th AIAA Fluid Dynamics Conference.

[23] Jameson, A., 1991. "Time dependent calculations using multigrid, with applications to unsteady flows past airfoils and wings". Fluid Dynamics and Co-located Conferences. American Institute of Aeronautics and Astronautics, Oct.

[24] Zha, G.-C., Shen, Y., and Wang, B., 2011. "An improved low diffusion e-cusp upwind scheme". *Computers & Fluids,* ***48***(1), pp. 214 – 220.

[25] Zha, G.-C., and Bilgen, E., 1993. "Numerical solutions of euler equations by using a new flux vector splitting scheme". *International Journal for Numerical Methods in Fluids,* ***17***(2), pp. 115–144.

[26] Im, H., Chen, X., and Zha, G., 2011. "Simulation of 3d multistage axial compressor using a fully conservative sliding boundary condition". pp. 1321–1330. IMECE2011-62049.

[27] Shur, M. L., Spalart, P. R., Strelets, M. K., and Travin, A. K., 2008. "A hybrid rans-les approach with delayed-des and wall-modelled les capabilities". *International Journal of Heat and Fluid Flow,* ***29***(6), pp. 1638 – 1649.

[28] Gan, J., Im, H.-S., Espinal, D., Lefebvre, A., and Zha, G.-C., 2014. "Investigation of a compressor rotor non-synchronous vibration with and without fluid-structure interaction". Vol. Volume 7B: Structures and Dynamics of *Turbo Expo: Power for Land, Sea, and Air*. V07BT35A018.

Copyright © 2020 by ASME